Detection of Precursors to Component Failure in a Spur Gear Drive-Train by Means of a Torque Transducer

Joseph Yutzy[1], Christopher Bruns[2], Nathanael Yoder[3], Douglas E. Adams[4], Kamran Gul[5], and Keith Calhoun[6]

[1, 2, 3, 4, 5] *Purdue Center for Systems Integrity, Purdue University, Lafayette, IN, 47905, USA*
jyutzy@purdue.edu
cjbruns@purdue.edu
ncyoder@purdue.edu
deadams@purdue.edu
kamrangul@gmail.com

[6] *Rolls-Royce Indianapolis*
Keith.A.Calhoun@rolls-royce.com

ABSTRACT

In the wind energy industry, gearbox failures are among the most costly and the most frequent, adding significantly to the operation and maintenance costs over the life cycle of the turbine. Despite significant improvements in the understanding of gear loads and dynamics, even to the point of establishing international standards for design and specifications of wind turbine gearboxes,[*] these components generally fall short of reaching their 20 year design life. In a significant number of gearbox failures, the primary bearing on the low speed shaft experiences faults in its operation, such as misalignment and movement on the mounts. To investigate the topic of gear health management, a fault detection approach is applied to a test bed involving a spur gear double-reduction transmission, outfitted with a torque transducer and tri-axial accelerometers on the bearing cases. The test bed is not a wind turbine gearbox – the gear arrangement is different and the gears are smaller compared to that of a typical wind turbine gearbox – but it does serve to test the modeling and fault detection methods proposed in this paper. Both baseline and faulted measurements are taken from the experimental set-up for data analysis. It is shown that the torque sensor provides an early indication of fault precursors, such as misalignment and decreased lubrication, while also maintaining the capacity to identify mature faults, such as chipped and missing gear teeth. The measurements are analyzed using statistical based methods – the Mahalanobis distance and Parzen discriminant analysis. These features for fault detection are then characterized at various operating speeds for each of the geartrain conditions of interest. An analytical model is created from first principles for verification of results and for simulation of the free and forced dynamics of the system.[**]

1 INTRODUCTION

Wind energy production, now at a five-year average annual growth rate of 39% (windpoweringamerica.gov), is quickly taking its place as the leading player in the renewable energy arena. As fossil fuel reserves continue to deplete, the need for more efficient and robust wind turbines increases. Condition monitoring plays a critical role in both increasing turbine efficiency and extending the operating life by facilitating better control strategies to avoid harmful operating conditions that augment unscheduled maintenance and decrease the turbine's productivity. Much work has already been accomplished as improved turbine design and control strategies have contributed to an increase in the average capacity factor from 22% (pre-1998) to 35% (installed turbine average from 2005-08) and beyond. (eree.energy.gov)

It has been shown that gearbox and generator failures are responsible for 17% of wind turbine failures while accounting for about 30% of the overall

---

[*] International Organization for Standardization, Wind Turbines – Part 4: Standard for Design and Specification of Gearboxes, ISO/IEC 81400-4:2005, ISO Geneva, Switzerland, February 2005.

cost of the system (Hyers *et al.,* 2006). These two factors combine to produce significant maintenance costs, making the drivetrain a prime candidate for condition monitoring. Hyers et al. note that vibration based condition monitoring has been demonstrated as capable of detecting damage to the gearbox, claiming that it "seems to be a solved problem." While this may be the case, the necessity remains for identification of the precursors, or causes of gear and generator faults, to extend the operational life of these components towards their design life because, as it stands, "most systems require significant repair or overhaul well before the intended life is reached" (Musial *et al.,* 2007). That is to say, it is well known that these faults occur and detection of these faults has been demonstrated. What remains to be clearly shown is the origin(s) of the frequent occurrence of these drivetrain faults.

As stated by Alban (1985), "It is very important, when studying a gear failure, that the examiner obtains an understanding of all possible environmental factors." Investigation of the causes of gearbox failures by Musial et al. reveals that gearbox issues are universal in nature, and not specific to any particular manufacturer. It also appears that poor adherence to standards is not the primary source of failure, because failures have remained prevalent even after the development and adoption of international wind turbine gearbox standards. Furthermore, Musial et al. noted that "It is reasoned that the accepted design practices that are successfully applied through other industrial bearing applications must be deficient when applied to wind turbine gearboxes." The source of failure also does not appear to stem from manufacturing quality because this only contributes to 10% of failures. The majority of wind turbine gearbox failures initiate in the bearings. In addition to this observation, it is also noted that each bearing location prone to failure fails with relatively low dependence on machine size, make or model. (previous paragraph, Musial *et al.,* 2007)

Musial et al. report all of the many factors to which these failures are not attributable, leading to the hypothesis that the potentially adverse and highly dynamic operating environment, illustrated in Figure 1, is the largest source of component failure because it is a shared operating condition among all wind turbines, causing bearing loads to exceed design specifications. Bearing failure directly and immediately affects shaft and gear alignment, which may result in extraordinarily high loads in related components leading to rapid failure (Fernandes, 1996). As Xu and Marangoni note, for long-term and trouble-free operations, "adequate shaft alignment is essential." Generally, tooth bending fatigue is accepted as the most common gear failure mode, but it occurs much more readily with the presence of incorrect assembly, misalignment, overloads and inadvertent stress raisers (Fernandes,

1996), all of which may result from bearing failure. Torsional vibrations also play a large role in accelerating tooth fatigue failure (Alban, 1985), and Figure 1 illustrates the torsional vibration in a wind turbine gearbox.

Another precursor to failure that is of concern in any geared system, particularly a gear system expected to last 20 years, is improper lubrication. Lubricated systems generally require regular maintenance to ensure the rolling contacts remain in a suitable state. Major modes of lubrication related failures include rubbing wear, scoring, and pitting. However, many strength related failures (such as tooth bending fatigue) are directly or indirectly influenced by lubrication (Mu, 1994).

This paper is a preliminary investigation of the identification of precursors to drivetrain faults and gear failures, namely misalignment and improper lubrication, as well as an investigation of the identification of the actual faults resulting from the precursors including chipped gear teeth and missing gear teeth. It is proposed that these sub-par operating conditions are just as observable and even, in many cases, more observable through the use of a torque transducer when compared to the use of accelerometers or other sensors. The torque sensor is shown to be capable of detecting faults in the gear train with the added benefit of insensitivity to external force input, which influences an accelerometer's translational type measurement, and with the benefit of increased sensitivity to misalignment. A double spur gear reduction test bench is used to simulate the sub-par operating conditions examined in this paper and a physics-based analytical model is also developed for validation of the experimental results.
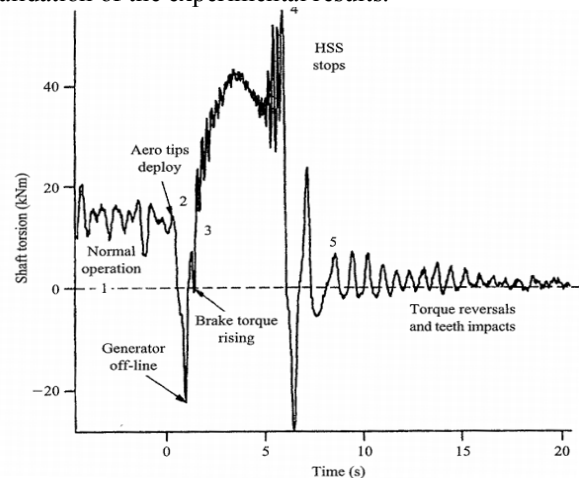

Figure 1: Dynamic, cyclic nature of torque in a wind turbine gearbox, different than most gearbox operating environments. This figure represents the shaft torsion experienced during braking. (Burton *et al.*, 2001)

2 ANALYTICAL MODEL

A model was developed to numerically describe and simulate the behavior of the gearbox being studied, given variations in the gearbox condition. This section of the paper discusses the methods used to model the gearbox being studied that is described in detail in the experimental procedure section. Once the model was fully developed, faults such as shaft misalignment and a chipped gear tooth were simulated by varying the model parameters. The methods applied here can be easily adapted to a wide range of gearbox applications.

The gearbox system was treated as a torsional elastic system consisting of a drive unit, couplings, a torque sensor, shafts, gears, and a brake. All of these components can be described with rotational stiffness parameters and lumped mass moments of inertia. Most of the system components are basic cylindrical shapes and were, therefore, easily modeled. For a cylinder, the rotational stiffness K is determined as follows:

$$K = \frac{T}{\theta} = \frac{G(I_o - I_i)}{L} = \frac{\pi}{2}\frac{G(r_o^4 - r_i^4)}{L} \quad (1)$$

where T is the torque on the cylinder, θ is the rotational deflection of the cylinder, L is the cylinder's length, G is the shear modulus, and I is the polar area moment of inertia given by $\pi r^4/2$ where r is the cylinder radius. Note that the subscripts o and i denote outer and inner radii, respectively, which allow for the calculation to be performed for a hollow cylinder (r_i is zero for a solid cylinder). The mass moment of inertia J was determined as follows:

$$J = \frac{\pi}{2}\gamma L(r_o^4 - r_i^4) \quad (2)$$

where γ is the density of the cylinder material.

Damping in the gearbox system was also accounted for in the model using stiffness-proportional damping. In most cases of simple rotational systems, stiffness-proportional damping models suffice to model the entire system with reasonable accuracy in terms of response amplitudes. The damping values can then be adjusted by correlating the model results with the experimental data once all other model parameters (inertia and stiffness) are determined.

The geared transmission system consisted of a series of rotating masses, $J_1, J_2,...,J_n$, attached to shafts of torsional stiffness, $K_1, K_2,...,K_{n-1}$, geared together with the average mean rotational velocities of the respective shafts and masses, $\omega_1, \omega_2,..., \omega_{n-1}$, and the corresponding rpm of the shafts $N_1, N_2,...,N_{n-1}$. The determination of torsional response characteristics are much simplified if the actual system is replaced by a dynamically equivalent system in which all masses and shafts rotate with the same speed with all gear ratios being 1/1, as shown in Figure 2.

In the equivalent system, each component should have the same kinetic energy and strain energy. These two constraints led to the following relationships between component i in the original system and its corresponding parameters in the dynamically equivalent system:
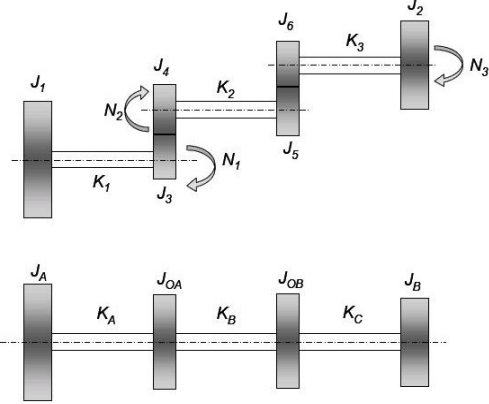

Figure 2: Example of dynamically equivalent torsional systems.

$$Kinetic\ Energy: KE_i = \frac{1}{2}J_i\omega_i^2 = \frac{1}{2}J_e\omega_e^2 = KE_e$$
$$J_e/J_i = (\omega_i/\omega_e)^2 = (N_i/N_e)^2 \quad (3)$$

$$Strain\ Energy: P_i = \frac{1}{2}K_i\theta_i = \frac{1}{2}K_e\theta_e = P_e$$
$$K_e/K_i = (\theta_i/\theta_e)^2 = (\omega_i/\omega_e)^2 = (N_i/N_e)^2 \quad (4)$$

Thus, the inertia J_e and stiffness K_e of each component in the dynamically equivalent system could be determined with reference to the equivalent system's speed, N_e. For example, referring to Figure 2, the equivalent inertias and stiffnesses, with reference to the equivalent system's speed, which was chosen to be $N_e=N_1$, are as follows:

$$J_A = J_1$$
$$J_{OA} = J_3 + J_4(N_2/N_1)^2$$
$$J_{OB} = J_5(N_2/N_1)^2 + J_6(N_3/N_1)^2$$
$$J_B = J_2(N_3/N_1)^2$$

$$K_A = K_1$$
$$K_B = K_2(N_2/N_1)^2$$
$$K_C = K_3(N_3/N_1)^2$$

Having modeled the simpler cylindrical components and determined their inertias and stiffnesses, the only components that remained to be included in the model were the gears. The inertia of each gear could be easily calculated by assuming the gears were simple cylinders and using the previously shown equation. However, in order to determine the torsional stiffness of each gear, a more complex model was needed.
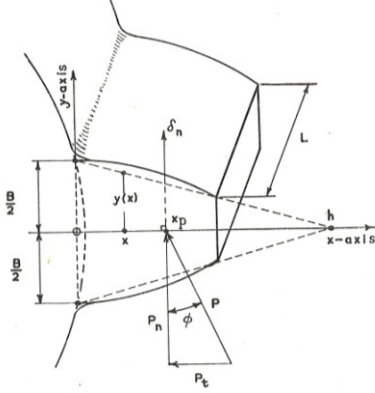
Figure 3: Gear tooth geometry and approximations. (Nestorides, 1958)

Many approximations of the torsional stiffness of spur gearwheels are available in the literature. Figure 3 shows the model of the gear tooth stiffness used for the system being analyzed (Nestorides, 1958). The linear compliance of the tooth was derived from the strain energy equation. The end result of the derivation was the linear stiffness of a gear tooth pair calculated as:

$$\frac{1}{K_L} = 2C\frac{12}{EL}\left(\frac{h}{B}\right)^3\left[2.3log_{10}\left|\frac{h}{h-h_p}\right| - \frac{h_p}{h}\left(1+\frac{h_p}{2h}\right)\right]+...$$
$$...+\frac{h_p}{GLB(1-h_p/2h)} \qquad (5)$$

where the correction factor C is 1.3 for spur gears. The correction factor is applied to account for the depression of the tooth surface at the line of contact and for the deformation in the part of the wheel body adjacent to the tooth. Additionally, E is the modulus of elasticity of the gear, G is the shear modulus, and $h, h_p, B,$ and L are the gear geometric properties as shown in the figure. The torsional stiffness of the gear tooth pair was then calculated as follows:

$$K = 2R^2K_L. \qquad (6)$$

Using the previously described techniques, the inertia and stiffness parameters of every system component are modeled. The overall dynamically equivalent system has 8 degrees of freedom (DOFs), and can be represented with a schematic as in Figure 4 where n=8.
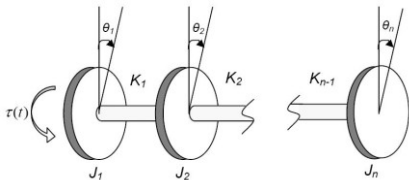

Figure 4: Simple schematic of modeling approach.

For the modeled system shown in the figure, the inertia and stiffness matrices are derived as follows:

$$[J]=\begin{bmatrix} J_1 & 0 & 0 & \cdots & 0 \\ 0 & J_2 & 0 & & \vdots \\ 0 & 0 & & \ddots & 0 \\ \vdots & & \ddots & J_{n-1} & 0 \\ 0 & 0 & \cdots & 0 & J_n \end{bmatrix}$$

$$[K]=\begin{bmatrix} K_1 & -K_1 & 0 & 0 & 0 \\ -K_1 & K_1+K_2 & -K_2 & 0 & 0 \\ 0 & -K_2 & \ddots & \ddots & 0 \\ 0 & 0 & \ddots & K_{n-2}+K_{n-1} & -K_{n-1} \\ 0 & 0 & 0 & -K_{n-1} & K_{n-1} \end{bmatrix}$$

with the overall system of equations of motion (EOM) expressed in matrix-vector form being:

$$[J]\{\ddot{\theta}\}+\underbrace{(I+j\eta)[K]}_{\triangleq[\bar{K}]}\{\theta\}=[T(t)] \qquad (7)$$

Here, I is an n by n identity matrix and $(I+j\eta)[K]$ is a complex stiffness matrix appropriate for use in forced torsional response calculations. As previously mentioned, this model consists of a linear discrete torsional system with n=8 DOFs, but this technique could be applied to a wide range of torsional systems and geartrains. The system components represented by each DOF are listed in Table 1.

Using modal superposition with the derived system EOMs, the torsional vibration natural frequencies (TNFs) and mode shapes were determined. The first two modal deflection shapes are shown in Figure 5 and the TNFs are tabulated in Table 2.

Table 1: System degrees of freedom denoted by node numbers and their corresponding system components.

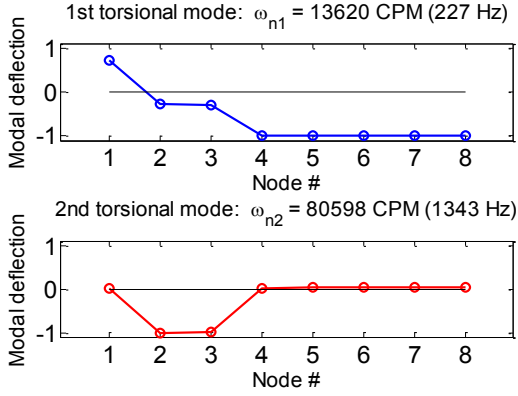| DOF (Node #)	Corresponding System Component
1	Motor
2	Coupling 1
3	Torque Sensor
4	Coupling 2
5	Gear Shaft 1 and Gears
6	Gear Shaft 2 and Gears
7	Gear Shaft 3 and Gear
8	Brake

Figure 5: First two Torsional Mode Shapes of the Test Bench.

Table 2: Torsional Natural Frequencies, calculated from the lumped parameter model.

Flexible Mode	Torsional Natural Frequency (Hz)
1st	0
2nd	227
3rd	1343
4th	4439
5th	7066
6th	8142
7th	12299
8th	16754

The frequency response functions (FRFs) were also computed to analyze the behavior of the first two modes, which are the only modes within a frequency range low enough to be excited by the gearbox system under normal operating conditions. The FRFs were computed using the following equation and are plotted in Figure 6.

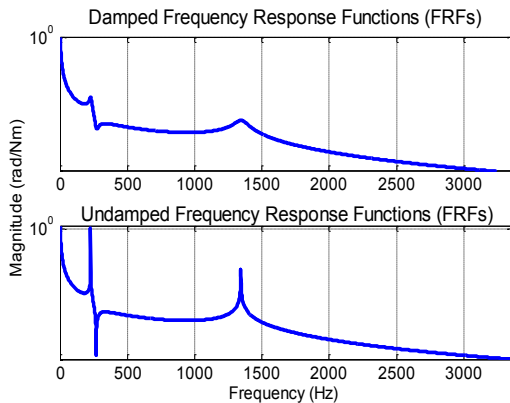$$[H(j\omega)] = \left[(j\omega)^2 [J] + (I + j\eta)[K] \right]^{-1} \qquad (8)$$

Figure 6: FRFs of lumped parameter model.

Having calculated the system's natural vibration characteristics, the operational conditions were then simulated. In order to capture the meshing frequency of the gear teeth during operation, it was necessary to consider the parametric vibration characteristics associated with the operation of gears. This analysis involved calculation of the contact force between the gears, which required use of the dynamic transition error (DTE). Though many complex models exist for this purpose (Wang *et al.*, 2003), a single degree of freedom model was chosen for modeling purposes in this paper. This model has been tested and proven to be adequate (Parker *et al.,* 2000). The schematic of the model that will be used is shown in Figure 7.
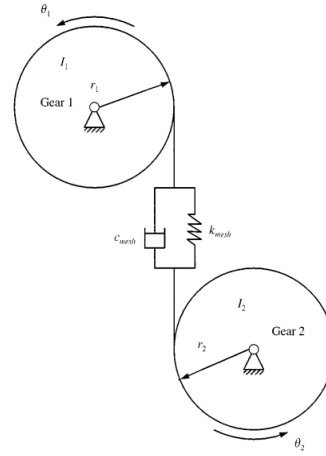
Figure 7: Single DOF system used to determine the DTE and contact for of the gear tooth mesh contact. (Parker *et al.*, 2000)

The EOM for this system is given below:

$$m\ddot{x} + c\dot{x} + F(t) = \frac{T_1}{r_1} = \frac{T_2}{r_2} \qquad (9a)$$

$$F(t) = \begin{cases} k(t)x, & x \geq 0 \\ 0, & x < 0 \end{cases} \qquad (9b)$$

where x represents the DTE and $x=r_2\theta_2+r_1\theta_1$. The system mass is $m=J_1J_2/(J_1r_2^2+J_2r_1^2)$. T represents the torque transmitted through the system and r is the radius of the pitch circle of the gear. The function $k(t)$ is the linear stiffness previously calculated times the number of gear tooth pairs in contact. The contact ratio (the average number of teeth in contact throughout a tooth mesh cycle) was used to calculate $k(t)$, which becomes a square wave as shown in Figure 8. Note that the varying width of the 2 teeth portion of the square wave was determined by the different contact ratios of each gear mesh; gear mesh 2 had a higher contact ratio and, thus, had 3 tooth pairs in contact for a larger portion of the tooth mesh cycle. The varying mesh stiffness, modeled here as a square wave, is a cause of

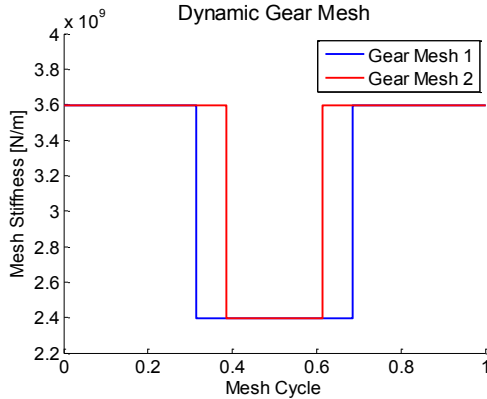the time varying nature of the operational dynamics of geared systems.

Figure 8: Rectangular wave approximation for the tooth mesh stiffness, *k(t)*, of both gear meshes in gearbox system being modeled.

The EOM for the single DOF tooth mesh model was solved using an ordinary differential equation solver in MATLAB that utilizes a fourth-order Runge-Kutta algorithm. Once the EOM was solved, the tooth mesh force was determined with the following equation where *f* is the tooth mesh force.

$$f = c\dot{x} + kx \qquad (10)$$

These tooth mesh forces cause torsional vibrations in the system demonstrated in a DTE sample that is shown in Figure 9.
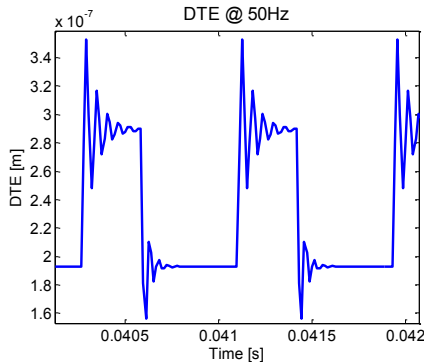

Figure 9: Sample of a gear mesh's Dynamic Transmission Error.

Finally, having modeled the free and forced response of the gearbox, faults could be simulated. Thus, the torque measured by the sensor during operation was simulated, including misalignment simulated at the motor DOF. The resulting spectrum of the simulated torque can be seen in Figure 10. Several important peaks were observed in the plotted simulated spectrum of the torque measured by the sensor. The 100Hz peak is at 2x the operating speed - typical in rotational systems and due to the simulated motor misalignment. Next, at 720Hz, a peak relating to the

14.4x meshing frequency of the second gear pair can be seen followed by a peak at 1200Hz which is the peak corresponding to the 24x meshing frequency of the first gear pair. The remaining peaks are harmonics of the aforementioned peaks. There also exist very small amplitude side bands around the peaks at +/- 100Hz intervals due to the misalignment, but they cannot be seen in the linear amplitude plot. These peaks should be visible in the experimental data, and they are, as can be seen in Figure 14.
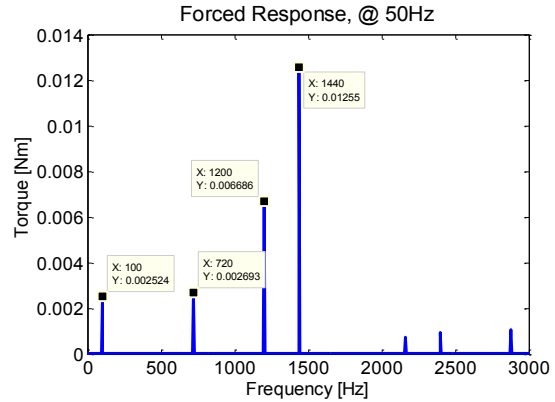

Figure 10: Forced response simulation of analytical model with misalignment.

It was also of interest to simulate the driveline response for a chipped tooth condition. Figure 11 represents the chipped tooth condition on the first gear (nearest the torque sensor in the drivetrain) in conjunction with misalignment. The chipped tooth was modeled as a 1 per rev decrease in stiffness, because a gear's tooth will become less stiff as a portion of its material is removed. This 1 per rev change excited the system's dynamics, particularly noted near the first TNF at 227Hz. These peaks are located at 50Hz, or 1x, increments.
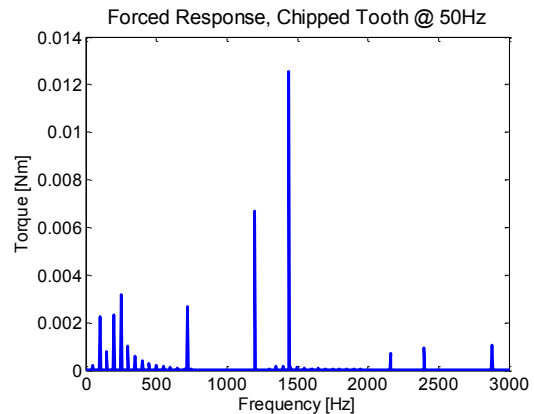

Figure 11: Forced response simulation of analytical model with misalignment and with a chipped tooth.

6

Several key results should be emphasized from the modeling. First of all, the location of the natural frequencies of the gearbox that were calculated will certainly play a role in the sensing the vibrations of the gearbox during testing. The resonances and anti-resonances as shown in Figure 6 will amplify and attenuate responses of the gearbox within certain frequency ranges. Second, the mesh frequencies should be observable in the experimental data as shown in the model. It is expected that these mesh frequencies will be significantly affected by faults in the gears corresponding to a particular mesh frequency, and thus these mesh frequency peaks will play a key role in fault identification. Finally, as shown in the model, the 2x frequency peak and its harmonics will be an important indication of misalignment in the gearbox. Overall, the simulation indicated that the torque sensor has the potential to measure the vibrations of the gearbox effectively. All of these key analytical results will be validated in the following sections.

3 EXPERIMENTAL APPARATUS AND DATA ACQUISITION

To investigate the prospect of identifying precursors to gear failure using a torque transducer, a test bench was purchased from Spectraquest® termed the Gearbox Dynamics System (GDS). While this test bench is different in size and gear arrangement from a wind turbine gearbox, it can be used to test and validate the modeling techniques already shown and the fault detection techniques which will be discussed. The system is shown in Figure 12, consisting of (L to R): Marathon® Electric D396 electric motor, a NCTE model Q4-50 torque sensor (±50 N·m), a two stage, parallel spur gear gearbox consisting of Martin Sprocket 14½° pressure angle gears of 2, 5, 3, and 4 inch pitch diameter (in drive order for a 5:1 speed reduction, input to output), and a Placid Industries magnetic particle brake B220. The GDS is additionally outfitted with two tri-axial PCB accelerometers, model 256A16 (100 mV/g nominal sensitivity). The accelerometers are placed on the outside of the gearbox housing with one near the input shaft and the other near the output shaft. Data was acquired through an Agilent E8401A VXI mainframe paired with an E1432A module sampling at 32.768 kHz. For measurement of shaft rotational speed, an optical sensor was placed on the input shaft between the motor and the first coupling.

The first data acquired consisted of motor run-up to provide a good overview of the drivetrain and its inherent dynamics. Multiple gear conditions were then introduced to the system for simulating either a faulted condition or a precursor or cause of geartrain failure. Faulted conditions considered were a chipped tooth and

a missing tooth and the precursors considered were misalignment (inherent in the test bench set-up) and lack of lubrication. The gear faults were introduced on the first gear in the drive order (closest to the torque sensor). Additionally, a data set was acquired with the simulation of external noise input through the use of a piezo-electric actuator, which was mounted to the gearbox casing. Except for the run-up measurement, steady-state data was collected at 5Hz motor speed increments, from 5-55Hz.
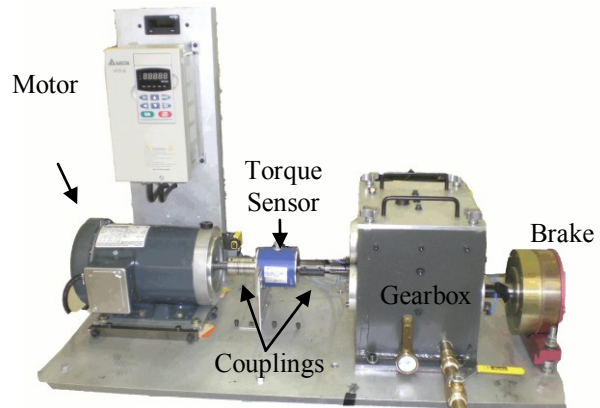

Figure 12: Double spur gear reduction test bench assembled by Spectraquest®.

4 EXPERIMENTAL DATA –VALIDATIONS

First, some validation of the numerical model was sought from the experimentally acquired data. The ramp-up data set was examined to reveal the principle dynamics of the system and to investigate their variation with speed. The spectrogram of this data is shown in Figure 13. This process revealed the analytical model's accuracy in predicting the TNFs of the system and confirms the presence of the first (24x) and second (14.4x) gear mesh frequencies as well as the first harmonic of the first mesh frequency (48x). Unbalance and misalignment (1-2x) are also demonstrated in the experimental data.
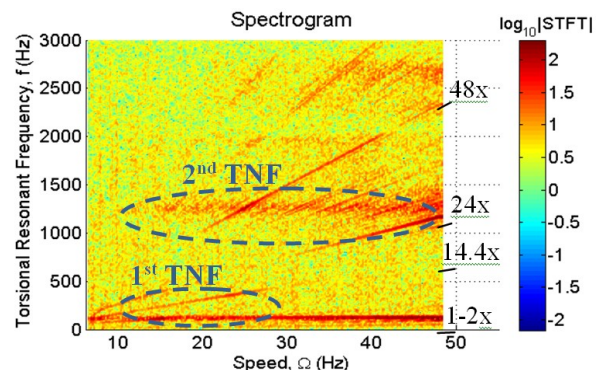

Figure 13: Spectrogram of speed sweep of the GDS.

Comparison between the accelerometer and torque measurements was also sought to investigate the suitability of the torque transducer in fault detection. Table 3 highlights the lesser variance in the torque data, as compared to the accelerometer, meaning a higher probability of fault detection due to the increased sensitivity to smaller changes. As previously mentioned, the torque data also reveals misalignment in the system, while the accelerometers were not observed to be as capable; this is shown in Figure 14. Also, the effect of external gearbox noise on the measurements is demonstrated in Figure 15. For this data set, the measurement is presented at a motor speed of 5Hz because higher operating speeds produce larger amplitudes of response, overshadowing the excitations due to the piezo-electric actuator. This data set makes it clear that excitations outside of the torsional system have little to no effect on the measured torsional dynamics, while the accelerometers are greatly affected in their measurement. The effect of external noise on the torque sensor and accelerometer measurements over all tested operating speeds is summarized in Figure 16. As can be seen in Figure 16, the mean value of the amplitude of the spectrum of the torque measurements (calculated using the Fast Fourier Transform with synchronously averaged data) is not increased by the added external noise. However, the accelerometer measurements are clearly impacted by the added noise, as the mean amplitude of the frequency content of the accelerometer signals increases due to the added energy input from the piezo-electric actuator. This property is something of consideration when choosing a transducer for an application like a wind turbine gearbox, where many other excitations (e.g. the wind, pitch/yaw actuators) are exciting the dynamics of the nacelle and surrounding components. Thus, a torque transducer appears to have an advantage over an accelerometer when measuring the dynamics of a rotational system in that the torque transducer is more sensitive to changes in the system (i.e. faults) as well as misalignment, and it appears to be insensitive to structure-born noise. However, in rotational systems sources of torsional noise also exist, such as variations in wind speed on the rotor of a wind turbine. The torque transducer will be affected by this torsional noise but will remain unaffected by translational structure-born noise occurring outside of the rotational system of interest, such as varying wind conditions creating vibrations in the nacelle of a wind turbine.

Table 3: Comparison of std. dev. of torque and accelerometer data at 55Hz.

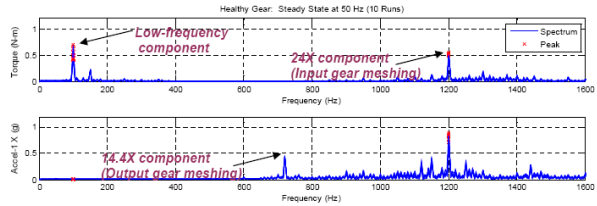| 55 Hz (Healthy vs. Faulty)	Torque	Accel-X	Accel-Y	Accel-Z
Shift in Mean $(\overline{x}_{Healthy} - \overline{x}_{Damaged})$	0.5624 (-85.4%)	-0.0072 (-11.0%)	0.0064 (-12.9%)	0.0988 (-60.7%)
St. dev., σ (Healthy)	3.7% of $\overline{x}$	36.2% of $\overline{x}$	10.6% of $\overline{x}$	19.2% of $\overline{x}$
St. dev., σ (Faulty)	21.6% of $\overline{x}$	47.7% of $\overline{x}$	36.1% of $\overline{x}$	50.9% of $\overline{x}$

Figure 14: Spectrum of torque sensor and accelerometer signals highlighting the torque sensor's high sensitivity to misalignment.
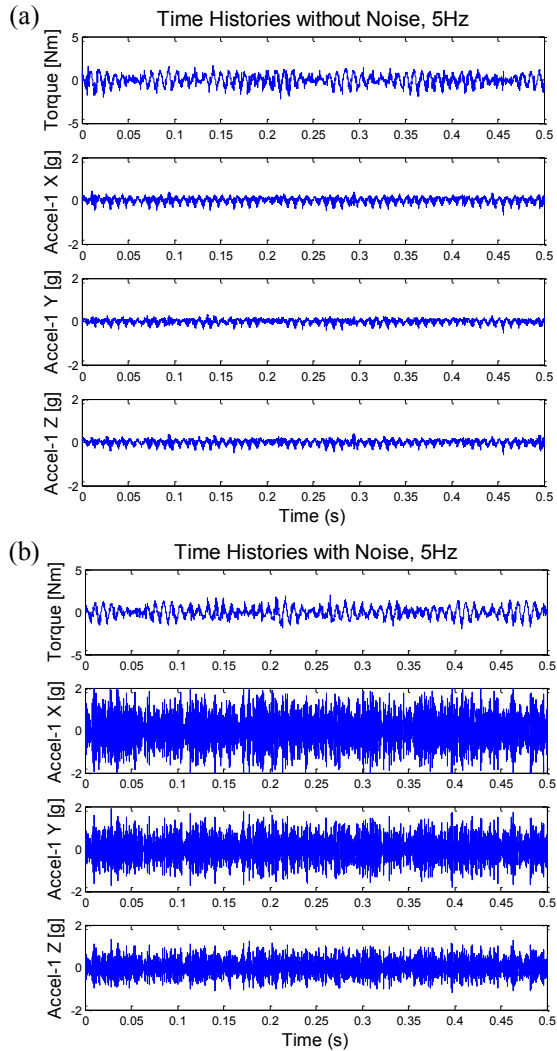

Figure 15: (a,b) Demonstration of the affect of external excitation on the measurement levels.
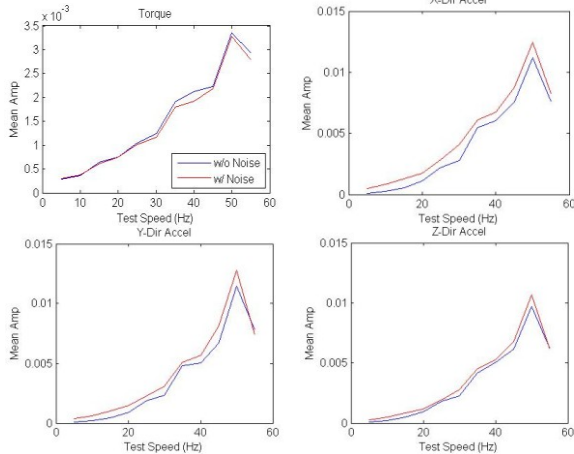
Figure 16: Mean amplitude of the frequency spectrum of the data plotted against operating speed for normal operation and operation with added external noise.

5   EXPERIMENTAL DATA ANALYSIS – STATISTICAL METHODS

The analysis of the steady-state operational data, to identify anomalies in the data, began with time synchronous averaging (TSA), which was performed to isolate the gear of interest and reduce noise. However, during this process it was determined that based upon the tachometer signal, the length of each duration drifted because of slight motor fluctuations. Typically, these variations are accounted for by interpolating the time histories so that they are all of the same length in an attempt to obtain samples that are at a consistent shaft angle. However, this process inherently assumes a piecewise constant shaft speed every rotation which results in shaft speed discontinuities. The shaft angle was consequently interpolated using cubic splines in order to obtain physically realizable shaft speed variations. Samples were then taken at constant shaft angles by interpolating the time history with cubic spline functions as well.

Using this interpolation methodology, TSA was performed based on 24 averages of a single input shaft rotation. To focus the following analyses on the 24 tooth gear on the input shaft, the magnitude of the frequency content of the TSA results at the 24x gear mesh frequency and the next 8 spectral points on either side were used to detect the presence of damage, resulting in a 17 dimensional damage feature vector. As mentioned in the analytical model section, the gear mesh frequency is expected to be significantly affected by faults in the gear corresponding to that particular mesh frequency (in this case the 24 tooth gear) and the surrounding 8 spectral points on either side will capture modulation of the fault in the surrounding frequencies. The mean 17 dimensional damage feature for each gear condition tested at an operating speed of 50Hz can be

seen in Figure 17. As expected, the main peak occurs at the center spectral component, which corresponds to the 24x gear mesh frequency. However, this peak shifts for the missing tooth condition due to the gear mesh being interrupted once per gear revolution by the missing tooth. The no lube condition results in increased noise in the torque signal, so the gear mesh frequency is not as defined and more modulation occurs. The baseline and chipped conditions are very similar with the exception that the baseline, or healthy, condition has higher amplitudes in the spectral components surrounding the gear mesh frequency. Similar patterns were seen in the damage features at other operating speeds.
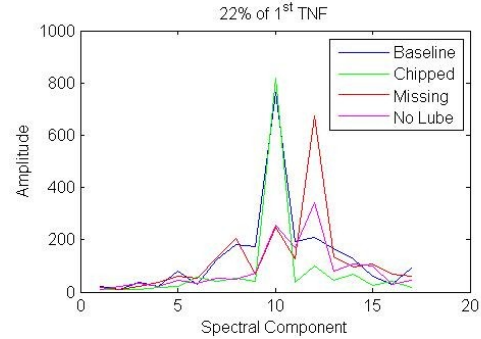

Figure 17: Mean 17 dimensional damage feature for each gear condition tested.

Each 17 dimensional damage feature vector was standardized by subtracting the mean and dividing by the standard deviation of the training data across each dimension. After calculating the standardized damage feature, an initial statistical analysis was conducted to investigate the feasibility of using the torque signal to detect when the system was no longer operating in the normal condition. To accomplish this task without the use of data from the damaged conditions, the Mahalanobis distance was used (Staszewski *et al.*, 1997). The Mahalanobis distance for a point $\mathbf{x}_k$ is calculated using the equation:

$$d^2(\mathbf{x}_k) = (\mathbf{x}_k - \boldsymbol{\mu})^T \boldsymbol{\Sigma}^{-1} (\mathbf{x}_k - \boldsymbol{\mu}) \qquad (11)$$

where $\boldsymbol{\mu}$ is the sample mean and $\boldsymbol{\Sigma}$ is the sample covariance matrix both of which are calculated using only the baseline data. Essentially, the Mahalanobis distance is a weighted measure of similarity that takes the correlations between variables in the baseline data set into account by using the first and second sample moments.

To set a detection threshold without the use of testing data, the mean and standard deviation of the Mahalanobis distances for the baseline data set were calculated. Because the distribution of the variables is very likely non-normal, the threshold was set at the mean of the Mahalanobis distances plus ten standard

deviations. By Chebyshev's inequality (Papoulis and Pillai, 2002), this means that regardless of the distribution from which this data comes, there is less than a 1% chance of data from this distribution being larger than the threshold.

In order to train the model, half of the healthy data was used for the baseline data while the other half was used to validate the model and determine if any number of false indications of damage occurred. As can be seen from the plots of the Mahalanobis distances at each of the investigated frequencies shown in Figure 18, no false indications of damage occurred and all of the other operational conditions could be distinguished from the healthy data. The data is plotted on a log scale because of the large separation between the healthy data and the data from any of the other conditions.

It is important to note the effects of the external noise (as previously discussed in section 4) on the Mahalanobis distance calculation. The resulting Mahalanobis distance from data for the baseline and missing tooth conditions with added external noise are presented in Figure 18. Ideally, the baseline, or healthy, data with the external noise would fall within the threshold set by the healthy data – or at least this should be true for torque sensor which should not be significantly affected by external translational vibration on the gearbox housing. As can be seen in Figure 18, this is not true, however the baseline data with noise is closer to the threshold relative to the other data sets for the torque measurements than for the accelerometer measurements. This indicates the torque sensor's lower sensitivity to translational structure born noise compared to the use of an accelerometer on the gearbox housing.

Overall, the Mahalanobis distance analysis successfully separated the healthy and damaged data, except for at 25 and 30Hz shaft speed. It is proposed that this is because the gear mesh frequency for input shafts speeds between 25 and 30Hz is between the first two calculated TNFs and therefore has a decreased signal to noise ratio. As previously described, a small test bench gearbox was used for the purposes of testing the methods presented in this paper; therefore, because of the importance of the TNFs to the response and the fact that both the TNFs and input shaft speeds of interest will decrease for larger gearboxes (e.g. wind turbine gearboxes), the data is labeled with the input shaft speed indicated as a percentage of the first torsional natural frequency in Figures 17, 18, and 19.
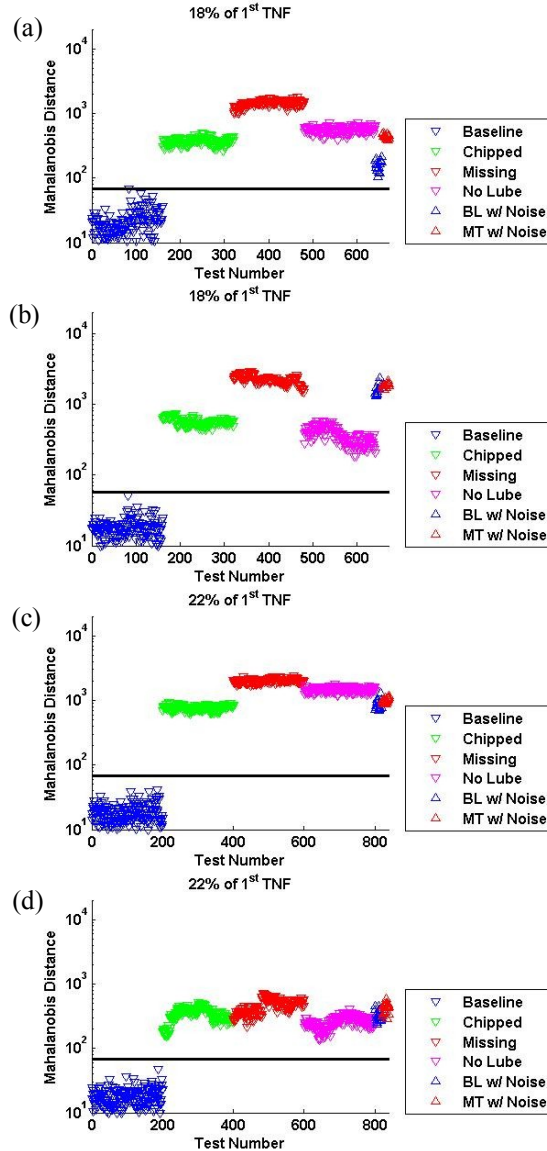

Figure 18: (a,b,c,d) Mahalanobis distance plots generated using half of the healthy data as the baseline case. The significant difference threshold is indicated with a black horizontal line. (a) and (c) are generated from torque sensor data, and (b) and (d) are generated from accelerometer data.

While this process enabled the healthy condition to be distinguished from the unhealthy conditions, it is unable to classify the type of damage. In order to facilitate this process, a two-step procedure was performed on the same data feature that was used for the previously described Mahalanobis distance procedure. Because this was a supervised learning process, half of the data from each condition was used as training data. Parzen discriminant analysis (Fang *et al.*, 2008) was then applied to the data. This analysis is a subspace projection method that makes no

assumptions about the underlying distributions of the data. Instead, it investigates local regions around each data point and attempts to maximize the ratio of the average local scatter across dissimilar groups (S_D) to the average local scatter within each group (S_S). This is achieved by solving the generalized eigenvalue problem:

$$S_D \mathbf{x} = \lambda S_S \mathbf{x}$$

$$S_D = \frac{1}{N} \sum_{i=1}^{N} \frac{1}{N_{R(\mathbf{x}_i)}^D} \sum_{\substack{\mathbf{x}_j \in R(\mathbf{x}_i) \\ c(\mathbf{x}_i) \neq c(\mathbf{x}_j)}} (\mathbf{x}_i - \mathbf{x}_j)(\mathbf{x}_i - \mathbf{x}_j)^T \quad (12b)$$

$$S_S = \frac{1}{N} \sum_{i=1}^{N} \frac{1}{N_{R(\mathbf{x}_i)}^S} \sum_{\substack{\mathbf{x}_j \in R(\mathbf{x}_i) \\ c(\mathbf{x}_i) = c(\mathbf{x}_j)}} (\mathbf{x}_i - \mathbf{x}_j)(\mathbf{x}_i - \mathbf{x}_j)^T \quad (12c)$$

where N is the total number of data points, $R(\mathbf{x}_i)$ is the local region around $\mathbf{x}_i$, N_{Rx}^D is the number of dissimilar samples in the region, and N_{Rx}^S is the number of samples in the region that are of the same class as $\mathbf{x}_i$ as indicated by $c(\mathbf{x}_i)=c(\mathbf{x}_j)$. The rows of the optimal projection matrix for a selected number of dimensions is then composed of the eigenvectors corresponding the largest eigenvalues. For this investigation, the data was projected down to two dimensions to ease visualization and the local region around each point, $R(\mathbf{x}_i)$, was defined as a hypersphere around each point whose radius was equal to five times the average distance to the nearest neighbor.

After the training data had been used to formulate the projection matrix described above, this matrix was then applied to the training data after which linear discriminant analysis (Johnson and Wichern, 2007) was performed on the projected data including data from the baseline and missing tooth condition with added external noise. This resulted in the correct classification of all testing data sets for the torque measurements without added external noise as can be seen in the classification scatter plots in Figure 19. The different classes (without the added external noise) are well clustered and separated at each of the input shaft speeds investigated for the torque data. However, the accelerometer data did not yield equally successful results at all operational speeds. For example, as can be seen in Figure 16b and 16d, the chipped tooth and no lube groups were not as distinct which led to several false classifications and similar results were seen at other operating speeds. Finally, it is important to note the effects of the external noise on this analysis. The baseline data with added noise was successfully classified in the baseline group when torque data was used (Figures 19a and 19c). However, the accelerometer data was not as successful at certain speeds (e.g. Figures 19b). The missing tooth condition with the added external noise was not successfully

classified using the torque or the accelerometer data which points to the need for further analysis and experimentation regarding the classification process and the effects of external structure born noise. Finally, it should also be noted that simply applying linear discriminant analysis to the raw data or the first several principal components failed to correctly classify all of the data sets which shows the utility of the nonparametric discriminant analysis.
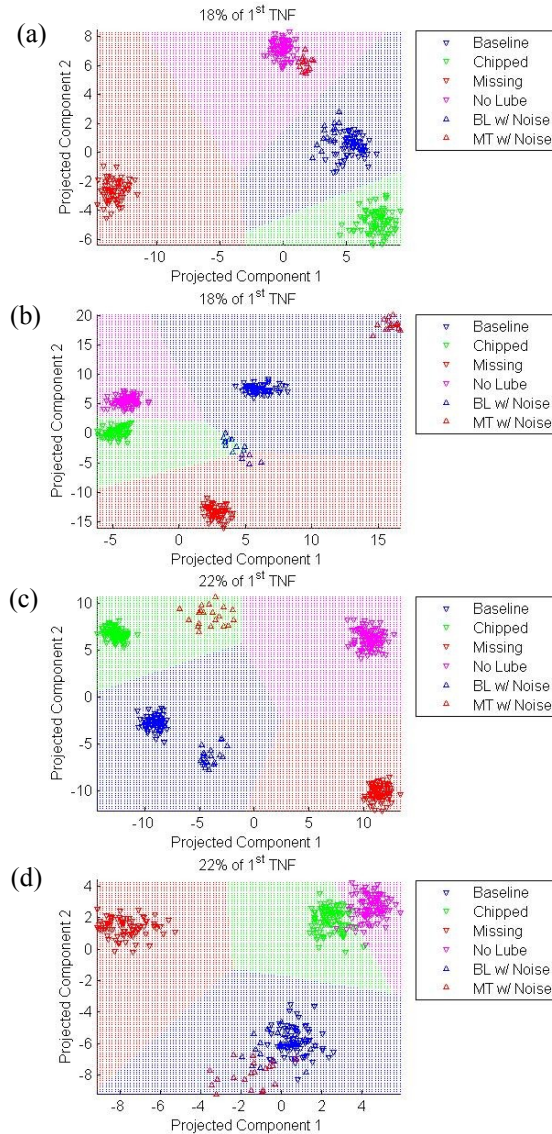

Figure 19: (a,b,c,d) The classification plots and boundaries generated using Parzen discriminant analysis to project the data into two dimensions and linear discriminant analysis to classify the projected data. (a) and (c) are generated from torque sensor data, and (b) and (d) are generated from accelerometer data.

6 CONCLUSION

A simple two-stage spur gear bench test was used for validation of a hypothesis endorsing the adeptness of torque transducer measurements in detecting drivetrain component faults. The numerical model was first shown to be capable of simulating the operational response measured by the torque transducer, and could be updated for simulation of drivetrain conditions of interest, knowing the condition's effect on the system properties. It has been shown through statistical methods and experimentation that a torque transducer is capable of detecting both drivetrain faults, namely chipped and missing teeth, and precursors to faults, namely misalignment and lack of lubrication. This could be useful in applications (such as a wind turbine geartrain) plagued with frequent gear failures, where detection of fault precursors is necessary to circumnavigate absolute failure. Through the application to multiple data sets of known conditions or faults, this method could be trained for use in any application. The torque sensor was additionally shown to be highly sensitive to low frequency vibrations due to misalignment and insensitive to ambient noise introduced to the gearbox housing – a noted advantage over accelerometers for use in gear trains, which operate in dynamic environments. The findings in this paper certainly seem to point to several advantages of the utilization of a torque sensor mounted to the driveline over accelerometers mounted to the gearbox housing in gearbox fault diagnostics, but further experimentation is necessary, as can be seen in the misclassification of the missing tooth condition when external noise was introduced (Figure 19). It is also important to remember that torque sensors are often difficult to install. Because of this drawback, future work involves exploring the possibility of a noncontact magnetic torque sensor, which would significantly improve ease of installation.

ACKNOWLEDGMENT

NOMENCLATURE

DTE	Dynamic Transmission Error
DOF	Degree of Freedom
EOM	Equation of Motion
TNF	Torsional Natural Frequency

G	Shear Modulus
I	Polar Area Moment of Inertia
J	Mass Moment of Inertia
K	Torsional Stiffness
L	Length
N_{Rx}^{D}	# of Dissimilar Samples
N_{Rx}^{S}	# of Samples in Class
$R(x)$	Local Region
S_D	Dissimilar Groups
Ss	Average Local Scatter
T	Torque
θ	Rotational Deflection
$k(t)$	Gear Mesh Stiffness
m	Gear Mesh Mass
μ	Sample Mean
r	Radius
Σ	Sample Covariance Matrix
x_k	Sample Point

REFERENCES

L.E. Alban (1986). Systematic Analysis of Gear Failures, *American Society for Metals*, Metals Park, OH.

T. Burton, D. Sharpe, N. Jenkins, E. Bossanyi (2001). Wind Energy Handbook. Wiley.

Y. Fang, S. Shan, H. Chang, X. Chen, and W. Gao (2008). Parzen Discriminant Analysis. In: Proceedings – 19th International Conference on Pattern Recognition. Tampa, FL.

P.J.L. Fernandes (1996). Tooth Bending Fatigue Failures in Gears. *Engineering Failure Analysis*. Vol 3. No 3. pp. 219-225.

R.W. Hyers, K.L. McGowan, K.L. Sullivan, J.F. Manwell, and B.C. Syrett (2006, September). Condition Monitoring and Prognosis of Utility Scale Wind Turbines. Energy Materials, Vol. 1, No. 3. pp. 187-203.

R.A. Johnson and D.W. Wichern (2007). Applied Multivariate Statistical Analysis. Pearson Prentice Hall.

P.M. Ku (1994). Gear Failure Modes – Importance of Lubrication and Mechanics. *ASLE Transactions*. Vol. 19, Issue 3. July 1976. pp. 239-249.

Walt Musial, Sandy Butterfield, and Brian McNiff (2007, May), in *Proceedings of European Wind Energy Conference*, Milan, Italy.

E.J. Nestorides (1958). A Handbook on Torsional Vibration. Cambridge University Press.

A. Papoulis and S.U. Pillai (2002). Probability . Random Variables and Stochastic Processes. McGraw-Hill.

R.G. Parker, S.M. Vijayakar, and T. Imajo (2000). Non-linear Dynamic Response of a Spur Gear Pair: Modelling and Experimental Comparisons. *Journal of Sound and Vibration* **237**(3), pp. 435-455.

W.J. Staszewski, K. Worden and G.R. Tomlinson (1997). Time-Frequency Analysis in Gearbox Fault Detection using the Wigner-Ville Distribution and Pattern Recognition. Mechanical Systems and Signal Processing. Vol. 11, No. 5. pp. 673-692.

J. Wang, R. Li, and X. Peng (2003, May). Survey of Non-Linear Vibration of Gear Transmission Systems. *Journal of Applied Mechanics*. Vol. 56. No. 3.

S. Watson and J. Xiang (2006, May). Real-time Condition Monitoring of Offshore Wind Turbines. in *Proceedings of European Wind Energy Conference*, Athens Greece.

M. Xu and R.D. Marangoni (1994). Vibration analysis of a Motor-Flexible Coupling-Rotor System Subject to Misalignment and Unbalance, Part 1: Theoretical Model and Analysis. *Journal of Sound and Vibration*. **176**(5), pp. 663-679.